HiSST: International Conference on
High-Speed Vehicle Science Technology

26–29 November 2018, Moscow, Russia

Interaction of Free and Bow Shock Waves with Local Gas Inhomogeneities

Pavel Yu. Georgievskiy[1], *Vladimir A. Levin*[2], *Oleg G. Sutyrin*[3]

Abstract

Interaction of free shocks waves and bow shocks ahead of blunt bodies with elliptical gas bubbles is studied numerically using two-dimensional axisymmetrical Euler's equations. Two distinct flow types — internal and external shock refraction patterns — are observed depending on flow parameters for both light and heavy bubble cases. For each case, shock focusing and cumulation process features and their effect on local force loads on the body are shown to depend on shock Mach number, bubble gas density and, most significantly, on bubble shape.

Keywords: *shock wave, supersonic flight, blunt body, gas bubble, shock focusing*

1. Introduction

Interaction of shock waves with local inhomogeneities takes place in wide range of problems, spanning from interstellar media processes and high-speed flight to supersonic combustion and inertial confinement fusion. The primary problem of this type is shock-bubble interaction (SBI), which has been a topic of study for several decades. Extensive experimental and computational studies, starting from the first experiments [1], demonstrated the a complex flow with shock focusing phenomenon [2] and formation of long-living vortex rings [3, 4, 5]. The flows are divided naturally into two major classes: the light and the heavy bubble cases. Although the shock focusing is present for the both cases, in the case of heavy bubble it is much more expressed and intense. In this scenario, for high bubble densities, there is an intense localized shock collapse followed by the formation of high-speed axial jets [5]. In latest years, a new research topic — shock-induced combustion of bubbles filled with a reactive gas mixture — was initiated in [6]. In almost all publications, only spherical gas bubbles were considered. In [7], we have studied shock focusing features for ellipsoidal bubbles and have shown that bubble shape plays very important — sometimes crucial — role in determining shock focusing pattern and intensity.

In study of interaction of blunt bodies with light gas bubbles in a supersonic ambient flow [8], intense pressure and density jumps at the critical point of the body were noted. The effect was presumed to be a result of cumulation of internal shock wave reflected from the rear bubble interface, but the mechanism of the cumulation was not fully revealed. Similar effects were observed later in numerical simulations of bow shock interaction with laser pulse energy deposition zones [9, 10].

The present work deals with the numerical study of shock focusing and cumulation effects for interaction of light/heavy gas bubbles with free shock waves and bow shocks ahead of blunt bodies and their effect on local body force loads.

2. Mathematical model and numerical method

The Euler equations with constant specific heat ratio γ are used to model unsteady two-dimensional axisymmetrical compressible gas flows:

$$\frac{\partial U}{\partial t} + \frac{\partial F}{\partial z} + \frac{\partial G}{\partial r} = H,$$

[1] *Institute of Mechanics of MSU, georgi@imec.msu.ru*
[2] *Institute of Mechanics of MSU, TsAGI, levin@imec.msu.ru*
[3] *Institute of Mechanics of MSU, TsAGI, sutyrin@imec.msu.ru*

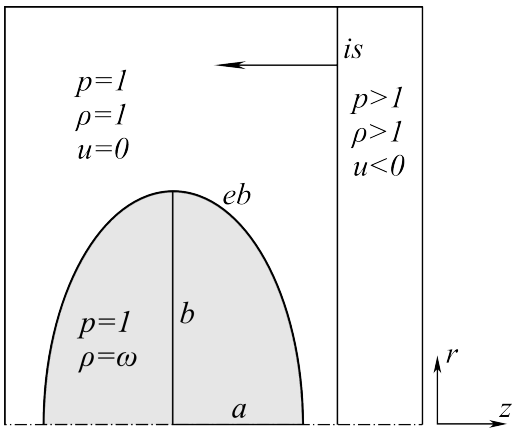

Fig 1. Flow schematic of the incident shock is propagating from right to left towards the elliptical bubble eb with gas density ω and axes a and b.

$$U = \begin{pmatrix} \rho r \\ \rho u r \\ \rho v r \\ e r \end{pmatrix}, \quad F = \begin{pmatrix} \rho u r \\ \left(p + \rho u^2\right) r \\ \rho u v r \\ (e+p) u r \end{pmatrix}, \quad G = \begin{pmatrix} \rho v r \\ \rho u v r \\ \left(p + \rho v^2\right) r \\ (e+p) v r \end{pmatrix}, \quad H = \begin{pmatrix} 0 \\ 0 \\ p \\ 0 \end{pmatrix}$$

Here p and ρ are the pressure and density respectively, u, v are the velocity components and e is the total energy per unit volume: $e = p/(\gamma - 1) + \rho(u^2 + v^2)/2$.

Numerical modeling was performed using the MacCormack explicit difference "predictor-corrector" scheme [11] of second-order accuracy:

$$U^{(1)}_{m,n} = U^k_{m,n} - \Delta t \left(\frac{F^k_{m+1,n} - F^k_{m,n}}{\Delta x} + \frac{G^k_{m,n+1} - G^k_{m,n}}{\Delta y} \right),$$

$$U^{k+1}_{m,n} = \frac{1}{2} \left[U^k_{m,n} + U^{(1)}_{m,n} - \Delta t \left(\frac{F^{(1)}_{m,n} - F^{(1)}_{m-1,n}}{\Delta x} + \frac{G^{(1)}_{m,n} - G^{(1)}_{m,n-1}}{\Delta y} \right) \right],$$

where (k, m, n) are indexes for (t, x, y) respectively and $F^{(1)}_{m,n}$ and $G^{(1)}_{m,n}$ are the values of $F_{m,n}$ and $G_{m,n}$ recalculated after the predictor stage. Stability of the scheme was ensured by applying the Courant-Friedrichs-Lewy condition with an additional safety factor of 0.6.

Non-physical oscillations near shock fronts were suppressed by introducing conservative artificial diffusion and anti-diffusion operators [12] after each time step:

$$\widehat{u}_i = (1 + A)(1 + D)u_i,$$

where u is a one-dimensional array to be monotonized and $\widehat{u}$ is the resulting array. D and A are diffusion and limited anti-diffusion operators respectively:

$$\begin{aligned} Du_i &= \varphi_{i+1/2} - \varphi_{i-1/2} = Q\delta u_{i+1/2} - Q\delta u_{i-1/2}, \\ \delta u_{i+1/2} &= u_{i+1} - u_i, \\ Au_i &= -\left(\varphi^c_{i+1/2} - \varphi^c_{i-1/2}\right), \\ \varphi^c_{i+1/2} &= s \max\left[0, \min\left(s\delta\widetilde{u}_{i-1/2}, \ \ |\varphi_{i+1/2}|, \ \ s\delta\widetilde{u}_{i+3/2}\right)\right], \end{aligned}$$

where $s = \operatorname{sign} \varphi_{i+1/2}$, $\widetilde{u}_{i+1/2} = (1 + D)u_{i+1/2}$ and Q is a constant parameter governing the relative intensity of the diffusion.
This procedure was applied successively for $\rho, \rho u, \rho v$, and e fields along both spatial dimensions after each time step.

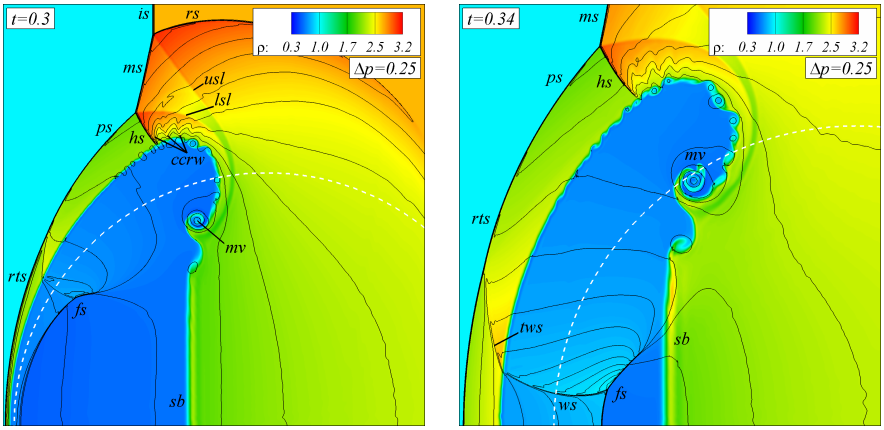

Fig 2. Free shock — light bubble interaction: density flood, pressure contours. Formation (left) and propagation (right) of a reflected focusing shock fs. rts — retransmitted shock, mv — main vortex, usl, lsl — upper and lower shear layers, respectively, $ccrw$ — centered compression-rarefaction waves.

3. Flow setup

A schematic of the initial flow condition for free shock case is shown in Fig. 1. The incident shock is is presented by a jump in normalized gas parameters between undisturbed gas ($p = 1$, $\rho = 1$, $u = 0$) and shocked gas ($p > 1$, $\rho > 1$, $u < 0$; the shock propagates from right to left), which are calculated using Rankine-Hugoniot conditions. The bubble is set as an elliptical area with the same pressure but different density ($p = 1$, $\rho = \omega \neq 1$) within the undisturbed gas area.

The top border of the studied area is a solid wall, and the bottom is the axis of symmetry, where the condition of symmetry $\partial/\partial r = 0$ is imposed. At the right border, a simple non-reflecting condition $\partial/\partial z = 0$ is implemented. The left border does not require any conditions to be set if no gas parameter disturbance reaches the border by the end of the simulation.

The governing parameters of the problem are the specific heat ratio $\gamma = 1.4$, incident shock Mach number M, ratio ω of the gas density inside the bubble to the ambient gas density (or Atwood number $A = \frac{\omega-1}{\omega+1}$) and bubble/blunt body geometry properties. Here, only one bubble geometry parameter — axle ratio e — is considered: $e > 1$ correspond to bubbles elongated along symmetry axis and $e < 1$ — to flattened ones. A uniform square computational mesh of 1200-1800 cells along the initial bubble diameter was used.

4. Shock — light bubble interaction

The light-bubble case ($\omega < 1,\ At < 0$) corresponds to a diverging shock refraction pattern in which the reflected wave is a rarefaction wave and the transmitted shock runs ahead of the incident shock. The shock compresses the bubble and deposits a significant amount of vorticity in the lateral area.

While the transmitted shock crosses the bubble edge, a retransmitted shock rts (connected to precursor shock ps) and a secondary, focusing shock fs form (Fig. 2, left). Similar secondary shocks have been observed for the interaction of a bow shock with a local energy deposition zone [13] and for the interaction of a shock with a light gas cylinder [14]. The focusing shock has a concave front; i.e., its central part propagates along the axis of symmetry while the outer counterpart propagates toward the axis. This "tilting" effect leads to the formation of a triple point and a relatively weak tertiary shock ws (Fig. 2, right). When the triple point reaches the symmetry axis, shock focusing (cumulation) occurs; i.e., a short local elevation of pressure and density on the axis. After the cumulation, fs eventually acquires a convex front and further propagates into the area behind the shocked bubble.

Depending on Atwood number At, Mach number M and bubble elongation $e = a/b$, shock focusing may

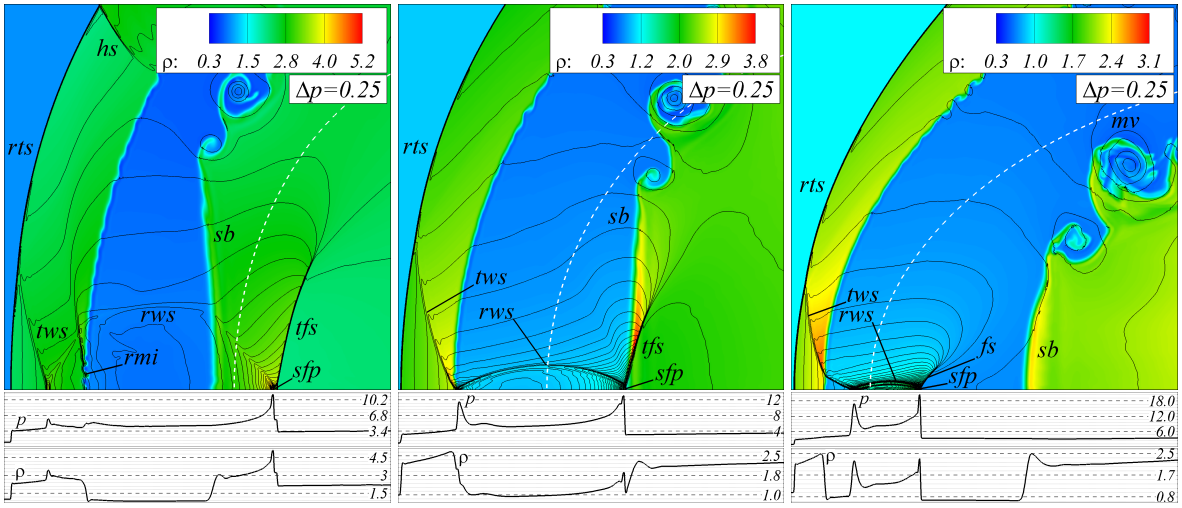

Fig 3. Shock focusing patterns in the example of $M = 2$, $\omega = 0.3$ $(At = -0.54)$; left to right: external $(e = 0.7)$, transitional $(e = 1)$ and internal $(e = 1.6)$. tfs — transmitted focusing shock, sfp — shock focusing point, rmi — local Richtmyer-Meshkov instability. The graphs at the bottom show the pressure and density distributions along the axis of symmetry within the corresponding z-coordinate region.

take place inside, outside or in the immediate vicinity of the edge of the shocked bubble (Fig. 3). Thus, it is possible to distinguish three qualitative shock focusing patterns (cumulation regimes): internal, external and transitional.

To acquire an approximate dependence of the shock focusing pattern features on At, M and e, a parameter study was performed for the following parameter ranges: $\omega = 0.7, 0.3$ $(At = -0.18, -0.54)$, $1.2 \leq M \leq 3$, and $0.5 \leq e \leq 2$. Consolidated charts for SFP patterns and intensities are given in Fig. 4. Each symbol represents a simulation for the combination of M, e; each chain of connected symbols corresponds to a set of simulation from the flattest ($e = 0.5$, leftmost symbol) to the longest ($e = 2$, rightmost symbol) bubble for constant M. The shock focusing pattern is coded by the background color: orange is external, yellow is transitional, and green is internal focusing pattern. The exact disposition of the borders between differently colored areas is not yet determined and they are drawn only schematically.

The dependence of the SFP pattern on Atwood number is minor: higher At correspond to a slightly earlier (in terms of following the symbol chain from left to right) transition from external SFP patterns to transitional and internal ones. At the same time, SFP dependence on M and e is quite strong. The general tendency is that oblate bubbles result in an external focusing while prolate bubbles end up in internal focusing. The SFP pattern for particular e depends on Mach number: for higher M, the transition from external to internal patterns occurs at higher e. One reason for this relation is the attenuation of the concavity of the focusing shock fs with an increase in M; the focal point of the less-concave shock lies farther behind the incident shock and thus farther from the bubble. The other, more significant reason is the intensification of the horizontal bubble compression; i.e., for higher M, the part of the axis of symmetry located inside the shocked bubble is shorter.

To compare the intensity of different shock focusing patterns, the pressure P_{foc} and density ρ_{foc} reached at the shock focusing point sfp were recorded as well. Under the present mathematical model, these parameters have notable dependence on grid resolution; an increase in grid resolution results in higher peak gas parameters reached upon shock focusing. Such absence of grid convergence for the SFP parameters is caused mainly by the absence of physical viscosity in Euler's equations; the only dissipation mechanism then is numerical viscosity, which decreases as the grid gets finer.

This issue significantly limits the present numerical approach in terms of its ability to determine exact

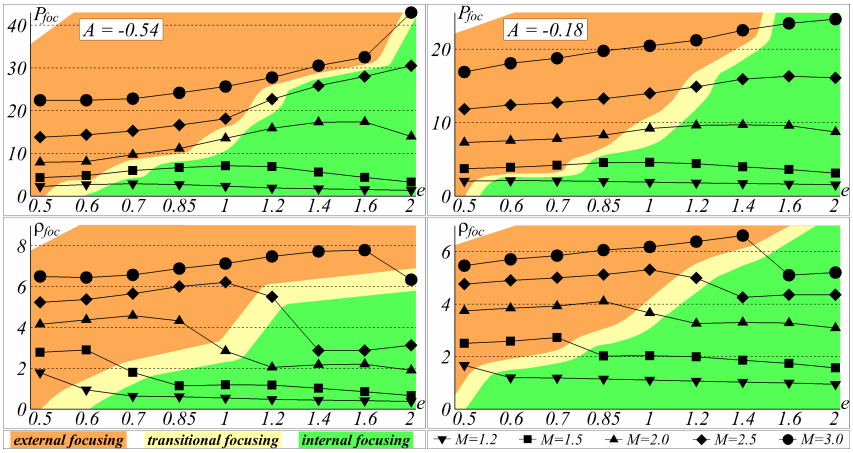

Fig 4. Peak pressure and density reached upon shock focusing for $\omega = 0.3$ (left) and $\omega = 0.7$ and different Mach numbers and bubble shapes. Red and green symbol backgrounds mark external and internal shock refraction patterns correspondingly.

gas parameters at shock focusing, but nonetheless does not prevent qualitative determination of the dependence of cumulative intensity on the flow parameters. To do so, the parameter study was performed twice: first for an 800×300 grid and then repeated for a 1600×600 grid; Although the values of P_{foc} and ρ_{foc} for individual grids were different, they demonstrated the same qualitative dependence on At, M and e under the each grid. Thus the relations described below may be considered to have physical significance.

The focusing pressure P_{foc} increases monotonically with e up to a point after the transition to the internal focusing pattern, at which a balance between the intensity and concavity of the focusing shock fs is reached. The focusing density ρ_{foc} reaches its maximum immediately before the transition to the internal pattern and then drops sharply; focusing takes place in the lighter gas inside the bubble. Thus, the most intense focusing patterns in terms of peak pressure are the internal ones, while the highest density is reached upon external focusing patterns that are closest to the point of transition between cumulation regimes.

If the shock is generated by supersonic flight of a blunt body, shock focusing and cumulation effects retain their qualitative features. Cumulative reflected shock arrives at the body near stagnation point on the symmetry axis, resulting in sharp pressure peaks in the local area and abrupt force loads on the body (Fig. 5). Similarly to free shock case, pressure peak significantly depends on M, ω and bubble shape. In some cases, non-spherical light gas bubble result in more intense shock focusing and higher local force load (Fig. 5, right).

5. Shock — heavy bubble interaction

The interaction of a shock with a heavy gas bubble ($\omega > 1$, $At > 0$) results in a converging shock refraction pattern (Fig. 6, left); owing to the higher gas density in the bubble, the transmitted wave falls behind the incident shock, while the latter diffracts around the bubble on the outside. The speed lag and the shape of the transmitted shock are greatly affected by all governing parameters— M, At, and e — and the shock refraction patterns inside the bubble are thus much more varied and complex than those in the light-bubble scenario. Although the junction between the incident and transmitted shocks at the bubble edge has only one pattern— regular with reflected shock— for all parameter combinations studied in the present work ($0.2 \leq At \leq 0.5$, $1.2 \leq M \leq 3$), patterns that are more complex, such as concave-forward refraction or Mach reflection [15] from the bubble edge, are expected to take place for higher Atwood numbers and/or even lower Mach numbers.

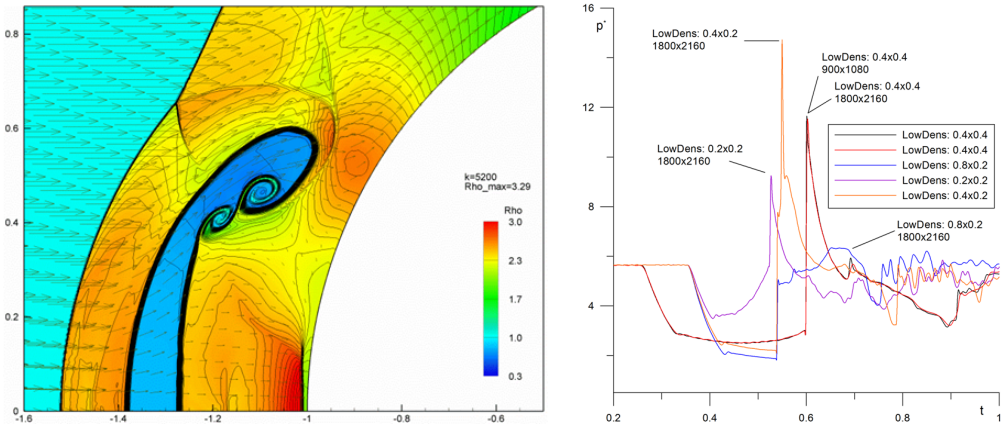

Fig 5. Blunt body — light bubble interaction: density and velocity fields. Arrival of cumulative shock on the body (left) and pressure oscillograms at stagnation point for different bubble shapes (right).

The reflected wave is a relatively weak shock rs. Its intensity is maximal near the axis of symmetry, where the flow corresponds to a one-dimensional Riemann problem, and gradually diminishes toward the edges. The transmitted shock ts has concave shape owing to the speed lag. Its outer part is formed by a transition of the incident shock through the lateral part of the bubble edge. Similar to the case for the reflected shock, the outer part of the transmitted shock is weaker than the central part.

As the transmitted shock propagates further, its concavity and intensity increase, and a triple point forms on its front, along with an outward-moving secondary shock oss and shear layer usl (Fig. 6, left). A similar turnover of the transmitted shock is observed for an interaction of a shock with an elliptical heavy gas cylinder [16, 17]. The length of the stem-like central part ts of the transmitted shock depends on At and e. In some cases, namely cases of very prolate bubbles with high Atwood numbers, the length may diminish to zero shortly after the formation of the triple point, similarly to the case of plane flow observed in [17].

In the majority of other cases, a second triple point appears on the transmitted shock (Fig. 6, right) later on. The second triple point is formed by the transmitted shock ts, inward-moving secondary shock iss, shear layer lsl and Mach stem ms that connects it to the first triple point. The interior part bis of the diffracting incident shock is propagates toward the axis, forming a nearly cylindrical shock convergence area. The outer part tss of the outward secondary shock oss is transmitted into the gas behind the bent initial shock bis, further contributing to distortion of the bubble.

As for the light-bubble scenario, the specific pattern of the subsequent shock focusing is heavily dependent on M, ω and e. If the transmitted shock ts leaves the bubble and retransmits into the undisturbed gas before the triple point reaches the axis of symmetry, external shock focusing occurs (Fig. 7, left); an area of high pressure/density forms outside the shocked bubble. In this case, a reflected expansion wave rew forms inside the bubble; the transmitted secondary shock tss overtakes the bent incident shock bis, forms a weak triple point wtp and retransmits ($rtss$) into the shocked bubble. A similar focusing regime for an interaction of a shock with an elliptical cylinder was denoted by a Type-II interaction in [16].

A transitional focusing pattern is characterized by convergence of two triple points with bent incident shock bis and collapsing of the resulting shock structure on the axis of symmetry in the immediate vicinity of the bubble edge (Fig. 7, center). This complex short-lived shock structure is formed within a small area near the axis of symmetry and thus represents a subject for further study using fine computational grids.

An internal pattern is characterized by the delay of formation of the second triple point and counter-propagation of several shocks: transmitted ts, upper transmitted uts, Mach stem ms and a part of

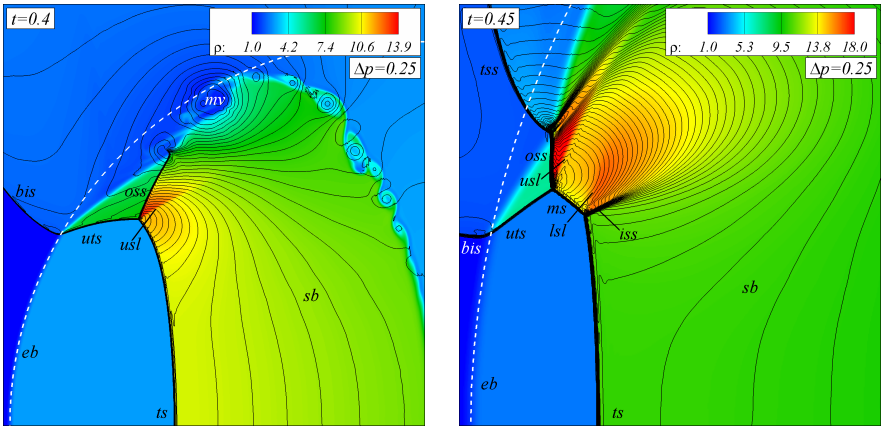

Fig 6. Free shock — heavy bubble interaction: density flood, pressure contours ($M = 2, At = 0.5, e = 1$). Formation of secondary cumulative shock and primary (left) and secondary triple points (right). is — incident shock, eb — elliptical-bubble edge, rs — reflected shock, ts — transmitted shock, sb — shocked-bubble edge, bis — bent (diffracted) incident shock, uts — upper transmitted shock, oss — outward secondary shock, usl — upper shear layer, mv — main vortex ring, tss — transmitted outward secondary shock, ms — Mach stem, iss — inward secondary shock, lsl — lower shear layer.

reflected incident shock ris. The moment shortly before their collapse is shown on the right of Fig. 7; propagation directions of the focusing shocks are shown by white arrows. This pattern corresponds to Type-I interaction of a shock with a gas cylinder observed in [16].

A parameter study was performed for the following parameter ranges: $\omega = 1.5$, 2, 2.5, 3 ($At = 0.2$, 0.33, 0.43, 0.5), $1.2 \le M \le 3$, and $0.5 \le e \le 2$. Unlike the light-bubble case, the pattern of interaction of a shock with a heavy bubble has notable qualitative dependence on gas density. All flows with the lowest density ratio ($\omega = 1.5$) resulted in external SFP pattern and thus are not presented here. The charts for the other cases are given in Fig. 8; similarly to the light-bubble case, the Mach number is coded by symbol shapes and focusing pattern by background color. The figure also includes square-shaped inserts that magnify a tightly-packed group of symbols near $0.85 \le e \le 1$ for $At = 0.50$.

The second lowest density ratio $\omega = 2$ ($At = 0.33$) also presents mostly external patterns and only one transitional, at $M = 1.2$, $e = 2$ (Fig. 8, left). A higher density ratio ($At = 0.43$, 0.5) leads to a wide variety of focusing patterns; the bubble elongation e becomes the most important parameter that governs the SFP pattern. At $At = 0.43$ bubbles with $e \ge 1.4$ undergo transitional cumulation almost independently of the Mach number (Fig. 8, center); the internal pattern is still rare and inherent mostly to the $M = 1.2$ cases. Internal regimes become common only at the highest studied density ratio (Fig. 8, right). Although less essential than in the light-bubble case, a Mach number between $M = 1.5$ and $M = 3.0$ still influences the SFP regime; an increase in M shifts the transition from an external to an internal focusing pattern toward slightly higher values of e, corresponding to more prolate bubbles.

In terms of shock focusing intensity, the interaction of a shock with a heavy bubble is qualitatively different from that with a light bubble. The original focusing shock is transmitted through the windward bubble edge rather than being reflected from the leeward edge and is thus much more intense. Because of this difference, the dependence of the peak gas parameters reached at the moment of shock focusing on the grid resolution is also greater. The indefinite P_{foc} rise with an increase in grid resolution results from the nature of the cylinder-like shock collapse; i.e., in the absence of dissipation, the focusing pressure of the ideal shock becomes infinite [18]. At the same time, density growth is limited. The peak density $\rho_{foc} \approx 193$ is many times higher than the theoretical peak density for a single shock $\rho_{max} = \frac{\gamma+1}{\gamma-1}\rho_0 = 6\omega = 18$ and yet is lower than the theoretical maximum achievable immediately after reflection of a converging spherical shock $\rho_{max} = 145\omega = 435$ [18].

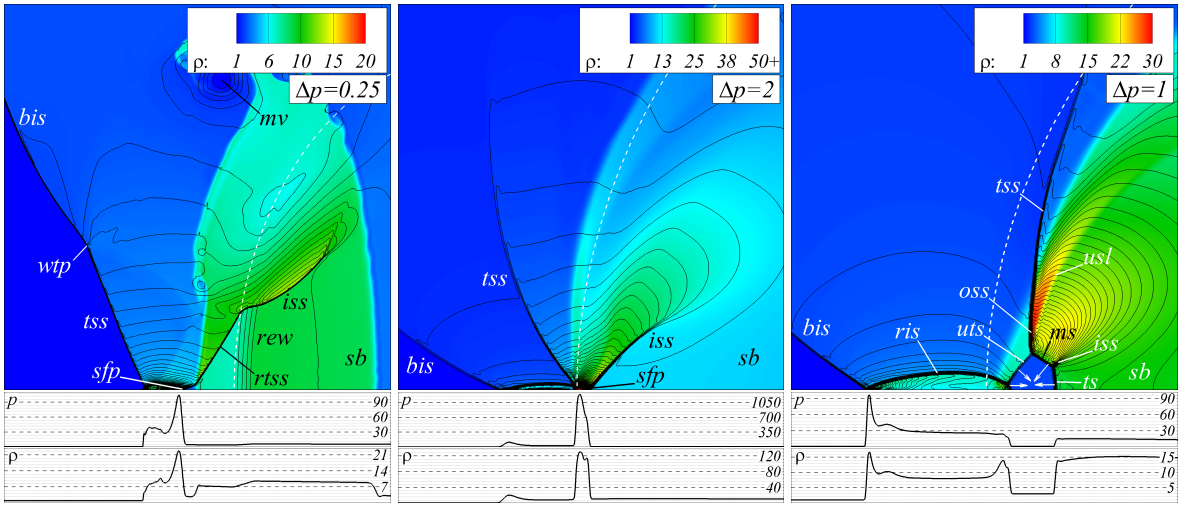

Fig 7. Shock focusing regimes in the example of $M = 3, \omega = 3\,(At = 0.5)$; left to right: external ($e = 0.6$), transitional ($e = 1.1$) and internal ($e = 1.4$, the time moment shown is shortly before the focusing). sfp — shock focusing point, wtp — weak triple point, rew — reflected expansion wave, $rtss$ — retransmitted secondary shock, ris — reflected bent incident shock. White arrows in the right-most figure indicate shock propagation directions.

Another obstacle in assessing real shock focusing parameters is the well-known effect of the instability of cylindrical or spherical shock convergence. Whether a similar effect plays a significant role in SBI may only be determined in proper three-dimensional simulations, and if there is in fact instability, the resulting focusing parameters are expected to be lower. Nevertheless, the present approach allows one to determine a qualitative dependence of the shock intensity on flow parameters. As in the light-bubble scenario, the parameter study was performed twice, for 800×300 and 1600×600 grids; Fig. 8 show the latter. For both grids, the shock focusing parameters demonstrated the same qualitative dependence on flow parameters.

Because of the convergent shock refraction pattern, even the weakest studied shock focusing regime— the external regime for $e = 0.5$ — produces a short tenfold rise in pressure/density, and the rise scales well with the Atwood number. With an increase in e, the shock focusing point approaches the bubble edge and both focusing parameters rise. Upon transition to the internal regime, P_{foc} and ρ_{foc} jump sharply. Due to the earlier transition from the external regime, in some cases less intense initial shocks may result in higher ρ_{foc} than more intense ones (see $e = 1$, 1.2 in Fig. 8, right).

Upon the interaction of fast-flying blunt body with heavy gas bubble, similar unsteady shock focusing and cumulation processes take place. The bubble pushes through the bow shock, heavily deforms and crashes into the body (Fig. 9, left), resulting in high local force loads near stagnation point. High intensity of local force load is the result of not only of the shock focusing process but also of gas cumulation — converging flow of heavy gas towards symmetry axis.

Conclusion

A numerical study of the interaction of a free or bow shock with elliptical gas bubbles was conducted. Two flow geometries — diverging (light bubble, $At < 0$) and converging (heavy bubble, $At > 0$) — were considered. The main object of interest was a shock focusing process for both geometries.

In the diverging case, a relatively weak focusing shock is generated by a reflection of the transmitted shock from the leeward bubble edge. The concave shape of the shock leads to the formation of a single triple point on its front and subsequent cumulation at the axis of symmetry. Three possible shock

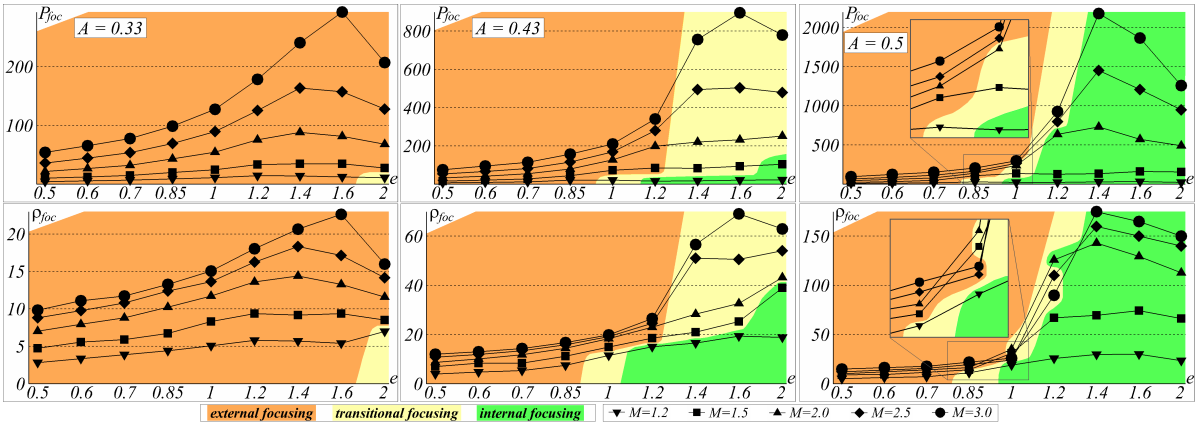

Fig 8. Shock focusing parameters for a heavy bubble at $At = 0.33, 0.43$ and 0.50. Each symbol corresponds to a single simulation; symbol shape represents Mach number and background color indicates shock focusing regime, as shown below the graphs. The border between different colored areas is drawn only schematically. Square-shaped insertions magnify an area near $0.85 \leq e \leq 1$, where symbols are tightly packed.

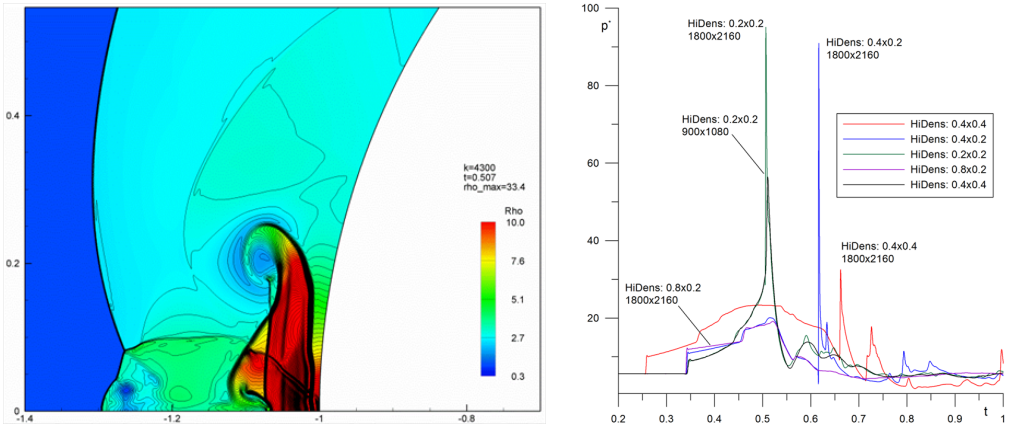

Fig 9. Blunt body — heavy bubble interaction: density field. Arrival of shocks on the body (left) and pressure oscillograms at stagnation point for different bubble shapes (right).

focusing patterns, distinguished by the position of the cumulation point relative to the shocked bubble, were found: external, internal and transitional.

In the converging case, the focusing shock is the transmitted shock itself. Again, three major shock focusing regime classes were found — external, transitional and internal. They differ not only by the position of the cumulation point but also by the shock patterns formed before the focusing takes place.

In the case of a supersonic flow past bodies fast implosion-type phenomena inside a shock layer result in dramatic pressure and density increasing in a focusing region. Shock focusing effects lead to the cumulation effect — intensive pressure and density jumps localized in a critical point of a body (stagnation point on the symmetry axis).

The research was supported by the Ministry of Education and Science (contract 14.G39.31.0001) and performed using the computational resources of the Supercomputing Center of Lomonosov Moscow State University.

References

[1] G. Rudinger L.M. Somers: Behavior of small regions of different gases carried in accelerated gas flows, J. Fluid Mech. **7**, 161—176 (1960)

[2] Picone J.M., Boris J.P.: Vorticity generation by shock propagation through bubbles in a gas, J. Fluid Mech. **189**, 23—51 (1988)

[3] J.-F. Haas, B. Sturtevant: Interaction of weak shock waves with cylindrical and spherical inhomogeneities, J. Fluid Mech., **181**, 41—76 (1987)

[4] G. Layes, G. Jourdan, L. Houas: Distortion of a Spherical Gaseous Interface Accelerated by a Plane ShockWave, Phys. Rev. Lett. **11**, 174502 (2003)

[5] D. Ranjan, J.H.J. Niederhaus, J.G. Oakley, M.H. Anderson, J.A. Greenough, R. Bonazza: Experimental and numerical investigation of shock-induced distortion of a spherical gas inhomogeneity, Phys. Scr., **T132**, 014020 (2008)

[6] N. Haehn, D. Ranjan, C. Weber, J. Oakley, D.Rothamer, R. Bonazza: Reacting shock bubble interaction, Combustion and Flame, **159**, 1339—1350 (2012)

[7] P.Yu. Georgievskiy, V.A. Levin, O.G. Sutyrin: Interaction of a shock with elliptical gas bubbles, Shock Waves, **25**(4), 357—369 (2015)

[8] Georgievskii, P.Yu., Levin, V.A.: Unsteady interaction of a sphere with atmospheric temperature inhomogeneity at supersonic speed. Fluid Dyn. **28**(4), 568—574 (1993)

[9] Yan, H., Adelgren, R., Bogushko, M., Elliott, G., Knight, D.: Laser energy deposition in quiescent air. AIAA J. **41**(10), 1988—1995 (2003)

[10] Schulein, A., Zheltovodov, A., Pimonov, E., Loginov, M.: Experimental and numerical modeling of the bow shock interaction with pulse-heated air bubbles. Int. J. Aerosp. Innov. **2**(3), 165—187 (2010)

[11] R.W. MacCormack: The Effect of Viscosity in Hypervelocity Impact Cratering, AIAA Paper **354** (1969)

[12] A.I. Zhmakin, A.A. Fursenko: On a Monotonic Shock-Capturing Difference Scheme, U.S.S.R. Comput. Maths. Math. Phys. **20** (4), 218—227, (1981)

[13] A.A. Zheltovodov, E.A. Pimonov: Numerical simulation of an energy deposition zone in quiescent air and in a supersonic flow under the conditions of interaction with a normal shock, Technical Physics, **58** (2), 170--184, (2013)

[14] A. Bagabir, D. Drikakis: Mach number effects on shock-bubble interaction, Shock Waves, **11**, 209--218, (2001)

[15] R. Nourgaliev, S. Sushchikh, T. Dinh, T. Theofanous: Shock wave refraction patterns at interfaces, Int. J. Multiph. Flow **31**, 969--995, (2005)

[16] J. Ray, R. Samtaney, N. J. Zabusky: Shock interactions with heavy gaseous elliptic cylinders: Two leeward-side shock competition modes and a heuristic model for interfacial circulation deposition at early times, Physics of Fluids, **12** (3), 707--716, (2000)

[17] M. Fan, Z. Zhai, T. Si, X. Luo, L. Zou, D. Tan: Numerical study on the evolution of the shock-accelerated SF_6 interface: Influence of the interface shape, China-Phys Mech Astron, **55**, 284--296, 2012

[18] G.B. Witham: Linear and Nonlinear Waves, Wiley, New York, (1974)